PCCP

PAPER

View Article Online
View Journal | View Issue

Cite this: *Phys. Chem. Chem. Phys.*, 2018, **20**, 12444

Correlated energy transfer in rotationally and spin–orbit inelastic collisions of NO($X^2\Pi_{1/2}$, j = 1/2f) with $O_2(X^3\Sigma_g^-)$

Zhi Gao, Tijs Karman, Guoqiang Tang, Ad van der Avoird, Gerrit C. Groenenboom and Sebastiaan Y. T. van de Meerakker*

Received 19th March 2018,
Accepted 18th April 2018

DOI: 10.1039/c8cp01784k

rsc.li/pccp

We present a combined experimental and theoretical study of state-to-state inelastic scattering of NO($X^2\Pi_{1/2}$, j = 1/2f) with $O_2(X^3\Sigma_g^-)$ molecules at a collision energy of 480 cm^{-1}, focusing in particular on the observation and interpretation of correlated excitations in both NO and O_2. Various final states of the NO radical, in both spin–orbit manifolds, were measured with high resolution using a crossed molecular beam apparatus which employs a combination of Stark deceleration and velocity map imaging. Velocity map imaging directly measures both the angular distribution and the radial velocity distribution of the scattered NO molecules, which probes the kinetic energy uptake or release and hence correlated excitations of NO–O_2 pairs. Simultaneous excitations of NO and O_2 were resolved for all studied final states of NO. In all cases, the experimental results excellently agree with the results of simulations based on quantum scattering calculations. Trends are discussed by analyzing the scattering wave functions from the calculations.

1 Introduction

It has been a long-standing goal in physical chemistry to probe potential energy surfaces (PESs), which govern intermolecular interactions. The study of inelastic collisions between molecules in the gas-phase is a well-established approach to this end. Combining the velocity map imaging (VMI) technique[1] and crossed molecular beam (CMB) technique,[2] the rotational energy transfer (RET) in atom-molecule collisions has been extensively studied.[3] In bimolecular inelastic collisions, the degrees of freedom of both molecules couple and therefore give rise to much more complex dynamics, when compared to atom-molecule collisions. The added degree of complexity offers opportunities to address dynamical questions including the so-called product pairs, *i.e.*, the simultaneous rotational excitation in both collision partners. By measuring product pairs, detailed information of the RET in both collision partner can be obtained. However, extending atom-molecule inelastic collision studies to bimolecular systems has remained challenging, and RET in bimolecular inelastic collisions is largely unexplored and not well understood.

On the experimental side, the main difficulty of studying bimolecular inelastic collisions compared to atom-molecule systems is the appearance of additional product channels from the simultaneous rotational excitation of both collision partners. Correlations between excitations of both colliders, referred to as product-pairs, may in principle be probed using VMI. Rotational energy transfer to or from the collision partner will result in a lower or greater kinetic energy, respectively. In VMI, one measures the velocity distribution, such that these different kinetic energies lead to a series of nested spheres,[4] whose projections on the two-dimensional detector yield a set of concentric circles. These circles in principle contain the full kinematic information of the collision process, including the integral and differential state-resolved correlated cross sections. It is, however, extremely challenging to experimentally resolve the individual circles, as the experimental blurring associated with, for instance, the collision energy spread and the crushing of spheres on the detector plane is in most cases much larger than the inherent spacing between the circles.[4–12] Recently, we reported the first observation of rotational product pair correlations in NO–O_2 inelastic collisions at a collision energy of 160 cm^{-1},[13] by using a Stark decelerator to produce reagent beams of NO with very narrow velocity spread.[14]

Here, we present a joint experimental and theoretical study of state-to-state resolved RET in the inelastic collisions of NO($X^2\Pi_{1/2}$, j = 1/2f) with $O_2(X^3\Sigma_g^-)$. As an extension of our previous experiment,[13] we study the dynamics at a higher collision energy of 480 cm^{-1} such that excitations of NO to higher rotational states can be probed. Furthermore, we study rotational excitation of NO within the $X^2\Pi_{1/2}$ (F_1) manifold, but we also study spin–orbit changing transitions to the $X^2\Pi_{3/2}$ (F_2)

Institute for Molecules and Materials, Radboud University, Heyendaalseweg 135, 6525 AJ Nijmegen, The Netherlands. E-mail: basvdm@science.ru.nl

manifold that is located 123 cm^{-1} above the F_1 manifold. As is well-known from studies of RET in collisions between NO and rare gas atoms or simple molecules,[15–32] the interaction between NO and its collision partner is governed by two non-adiabatically coupled PESs. Spin–orbit conserving $F_1 \rightarrow F_1$ transitions probe the average of the two PESs, whereas spin–orbit changing $F_1 \rightarrow F_2$ transitions are governed by the difference of the two PESs.[33–37] For all transitions, VMI images are recorded in which individual rings pertaining to NO–O_2 product-pairs are clearly resolved. The experimental results are in excellent agreement with the cross sections derived from quantum scattering calculations. From these calculations, we can rationalize trends that are observed in the pair-correlated cross sections.

2 Experimental and theoretical methods

2.1 Experimental set-up

The experiments were performed using a crossed molecular beam apparatus, containing a Stark decelerator and VMI detector, that is schematically shown in Fig. 1 and was described in detail before.[38] A mixture of 5% NO seeded in Kr at typical pressure of 1 bar is expanded through a Nijmegen Pulsed Valve (NPV)[39] and loaded into a 2.6 meter long Stark decelerator. After passing though the decelerator, a packet of NO($X^2\Pi_{1/2}$, j = 1/2f) radicals with a mean velocity of 430 m s^{-1}, a velocity spread of 2.1 m s^{-1} (1σ) and an angular spread of 0.1° (1σ) is scattered by a pulsed beam of neat O_2 at an intersection angle of 90°.

The O_2 beam is produced by expanding pure O_2 at a typical pressure of 3 bar though a NPV. The $O_2(X^3\Sigma_g^-)$ rotational energy level diagram is shown in Fig. 2. Each rotational state is labeled by the quantum number N, and is split by spin–spin and spin–rotation coupling[40] into three components labeled by the quantum number j with $j = N - 1$, N and $N + 1$. The initial rotational state distribution of O_2 was probed by measuring a (2 + 1) resonance enhanced multiphoton ionization (REMPI) spectrum. Fig. 2 shows the comparison between the measured spectrum and a spectrum simulated by PGOPHER[41] using a rotational temperature of 10 K. From this comparison we conclude that the O_2 molecules emerge from NPV predominantly in the N = 1 state, with a small amount of O_2 in the N = 3 state.

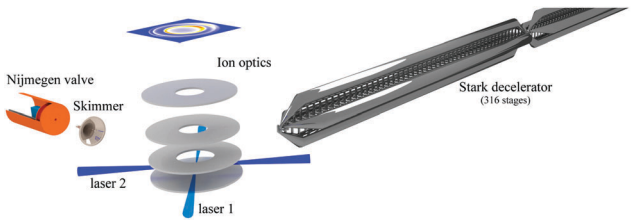

Fig. 1 Schematic representation of the experimental set-up. A 2.6 m long Stark decelerator is used to prepare a velocity controlled packet of NO radicals that is scattered with a pulsed beam of neat O_2 at 90° angle of incidence. The inelastically scattered NO are state-selectively ionized using two pulsed lasers, and recorded using a standard velocity map imaging detector. Only the last section of the Stark decelerator is shown here.

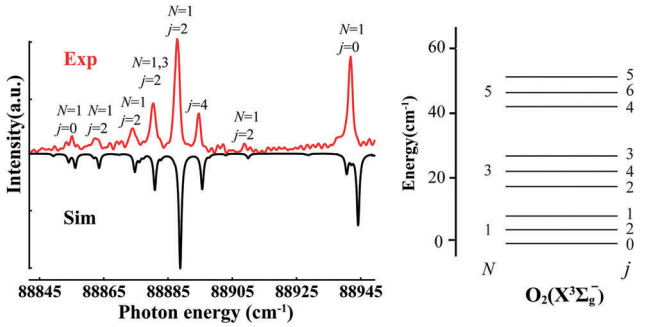

Fig. 2 Left: Comparison between experimental (Exp) and simulated (Sim) REMPI spectrum of O_2. The simulation assumes a rotational temperature of 10 K; the peaks are assigned by the rotational angular momentum (N) and total angular momentum (j). Right: The rotational energy level diagram of O_2, containing the three lowest N levels. The splitting of each rotational level into three j components is exaggerated for clarity.

The NO radicals were state-selectively ionized by a (1 + 1′) REMPI scheme using two pulsed dye laser systems. After ionization, the NO ions were collected by VMI optics. The collision energy was calibrated using the method described by Onvlee *et al.*,[28,38] and determined to be 480 cm^{-1}.

2.2 Quantum scattering calculations

Quantum mechanical scattering calculations were performed using the coupled-channels method. The details of the calculations are discussed in detail in ref. 13, and specific details are given here for completeness. The *ab initio* coupled potential energy surfaces were taken from ref. 13. These have been calculated using coupled cluster theory for the diagonal potential, and multi-reference configuration for the off-diagonal potential. The transformation to the diabatic representation has been determined using the multiple-property-based algorithm of ref. 42. The basis set used in the scattering calculations was truncated by the requirement $j_{NO} \leq 17/2$ and $N_{O_2} \leq 7$, total angular momenta up to $\mathscr{J} = 401/2$ were included, and the radial grid extended from 4.5 to $30a_0$ in steps of $0.05a_0$. Matching to scattering boundary conditions at the last grid point yields the S-matrices, from which the relevant DCSs are computed. Unlike what is described in ref. 13, we did not use the recoupling approach to compute fine-structure resolved cross sections, as the fine structure is not resolved experimentally and this treatment complicates the subsequent simulations.

We note that channels with N_{O_2} = 9 and 11 are also energetically accessible in the experiment, but their inclusion in the scattering calculations was not considered, as this would hugely increase both CPU time and memory requirements.

3 Analysis and simulation

3.1 Analysis method

The experimental scattering images were analyzed as described in more detail in ref. 13. We here only briefly describe the method for completeness, by illustrating the procedure using a scattering image as displayed in Fig. 3a as an example. This image pertains to

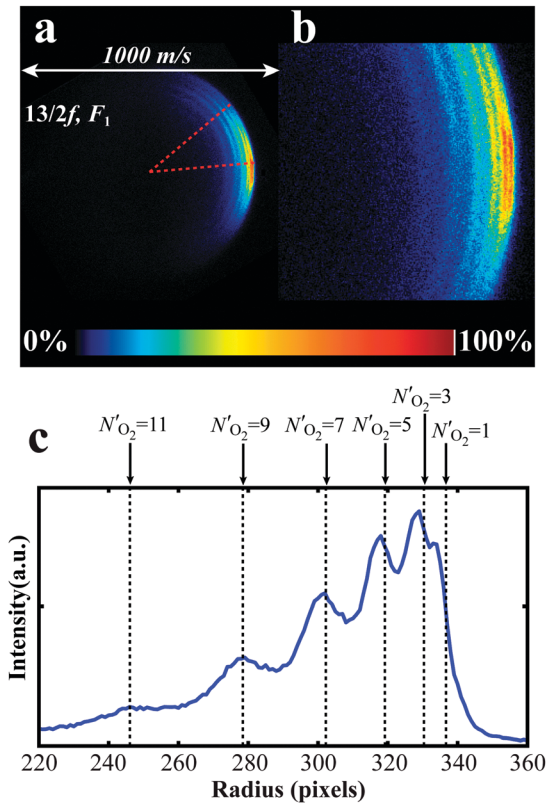

Fig. 3 The radial distribution of the scattering image pertaining to the inelastic process $NO(1/2f, F_1) + O_2(N_{O_2} = 1) \rightarrow NO(13/2f, F_1) + O_2(N'_{O_2})$. (a) Experimental VMI image. The image is presented such that the forward direction is located on the right-hand side of the image. The red dashed lines represent the angular segment in which the radial distribution is analyzed. (b) An enlarged representation of the forward part of the image. (c) The radial scattering distribution as obtained from the image. The vertical dashed lines represent the expected radii for different final states of O_2 (labeled at the top) based on the kinematics of the experiment.

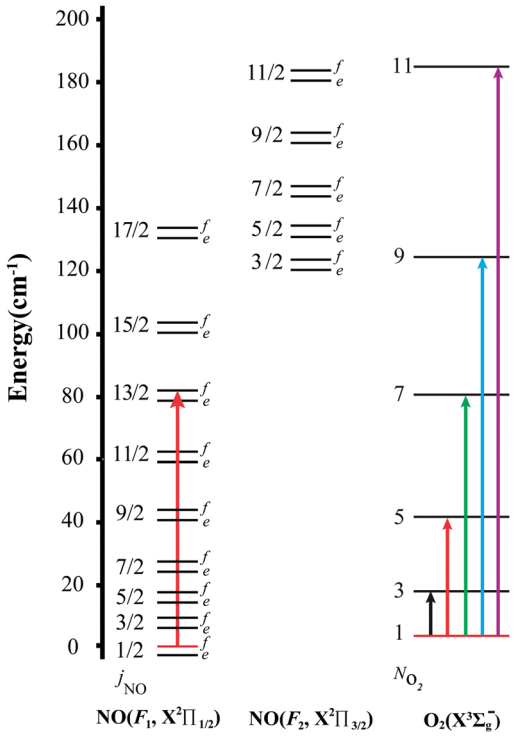

Fig. 4 The rotational energy level diagram of NO (left) and O_2 (right). The Λ-doublet splitting of NO is exaggerated for clarity, and the fine structure of O_2 is neglected.

excitation of NO into the $j'_{NO} = 13/2f$ state, as is also indicated by the red arrow in the energy level diagram shown in Fig. 4. In the collision process, the collision partner O_2 can be excited simultaneously to various rotational states $N'_{O_2} > 1$, as indicated by the set of colored arrows in Fig. 4. The multiple rings visible in the experimental scattering image correspond to these various scattering channels.

In order to assign the pair-correlated rotational excitations of O_2, the radial scattering distribution is analyzed within the angular range enclosed by the two red dashed traces, between -40° and -5°, simply by integrating the scattering intensity as a function of the radius R. This angular window was chosen as the radial resolution and scattering intensities are optimal here, while it avoids the forward scattering region that may be contaminated by unwanted initial population in the primary NO packet. Fig. 3c displays the radial distribution obtained from image a. The various rings can be assigned by comparing the radial distribution with the expected ring positions based on energy and momentum conservation. These positions, referred to as the kinematic cut-off positions, are indicated by the vertical dashed lines, together with the corresponding label N'_{O_2} for the final rotational state of O_2. It is seen that the maximum in intensity of the observed rings in the scattering image is shifted by 1 to 2 pixels inwards with respect to the kinematic cut-off. This shift is a result of both the projection of the three-dimensional Newton sphere onto two-dimensional detection plane and of the velocity spread of O_2 beam, and is fully accounted for in simulations of the experiment.[13] This shift, however, does not prevent the unequivocal assignment of the pair-correlated scattering channels in the experimental image.

For each ring, the angular distribution is analyzed using conventional methods as described before. Briefly, a circular annulus of a few pixels wide is defined. The scattering intensity within this annulus is then integrated, and evaluated as a function of the scattering angle θ.

3.2 Simulation

To compare the experimental results with theoretical predictions, we perform full simulations of the VMI images, based on cross sections from quantum scattering calculations. These simulations take all experimental conditions into account, such as beam spreads, temporal overlap, ionization volume, and spectral width of the laser.[28] The resulting simulated images are analyzed in an identical way as the experimental VMI images, such that radial and angular distributions can be directly compared. Since most O_2 molecules in the primary beam reside in the $N_{O_2} = 1$ state, we only take this initial state into account in our simulations. For a given final state of NO (j'_{NO}), we first simulate a scattering image for each of the possible $N_{O_2} = 1 \rightarrow N'_{O_2}$ transitions individually,

taking the appropriate DCS for the transition, and finally add all images together. Since in the quantum scattering calculations only O_2 states up to $N_{O_2} = 7$ could be included, we limit the simulations for each j'_{NO} state to the four product-pair channels $N'_{O_2} = 1, 3, 5, 7$. It is noted that some experimental images clearly contain signal for $N'_{O_2} = 9$ and 11 (see Section 4), and this is thus unaccounted for in the simulations.

As mentioned before, the calculations presented here do not include the O_2 fine structure components j_{O_2}. Each rotational transition, $N_{O_2} \rightarrow N'_{O_2}$, in principle consists of 9 fine-structure-resolved transitions, $N_{O_2}, j_{O_2} \rightarrow N'_{O_2}, j'_{O_2}$. These are not resolved experimentally, but the difference in excitation energy does contribute to a broadening of the observed rotational transitions. This effect is therefore also unaccounted for in our simulations.

4 Results and discussion

4.1 Spin–orbit conserving transitions of NO

Fig. 5 displays the experimental and simulated VMI images of NO molecules for spin–orbit conserving ($F_1 \rightarrow F_1$) transitions. Excitation of NO up to $j'_{NO} = 17/2$ was probed. Both final states of e and f parity were probed, in so far as isolated REMPI transitions were available to probe these levels. All images are presented such that the forward direction appears on the right-hand side of the images. For low values of j'_{NO}, small segments of the images around the forward direction are masked because of the imperfect state selection of the NO packet. It is seen that multiple rings are clearly resolved in all images. Furthermore, the relative intensity of the rings in each image depend strongly on j'_{NO}. For $j'_{NO} \leq 7/2$, the inner rings in the images are much weaker than the outermost ring, indicating that elastic scattering of O_2 is preferred over inelastic scattering. For higher values of j'_{NO}, the inner rings become more intense and inelasticity in O_2 gains importance.

Overall, the experimental images show excellent agreement with the simulated images, both in terms of the relative intensities of the rings and in terms of the angular distributions. This is quantified further by the radial profiles presented in Fig. 6, and by the angular profiles presented in Fig. 7. For the latter, we only present the angular distributions for the $N_{O_2} = 1 \rightarrow N'_{O_2} = 1$ outer ring, as for a given value for j'_{NO}, we observe only marginal differences in the angular distributions of the different rings. In the radial distribution for the 11/2e channel, one can observe an additional outer ring which is not present in the simulations. This additional ring is an experimental artefact that is caused by partially overlapping REMPI transition probing the 5/2f level. It is noted again that our simulations exclude excitations of O_2 into the $N'_{O_2} = 9$ and 11 levels (although they are clearly visible in the experimental profiles), and they exclude the fine-structure splitting of the O_2 transitions. The latter one causes the radial profiles to be consistently broader in the experimental results when compared to the simulations. From the radial and angular distributions, interesting trends can be discerned. As j'_{NO} increases, inelasticity in O_2 indeed gains significant importance, as was already apparent from visual inspection of the images in Fig. 5. In addition, the angular distribution shifts from forward scattered to sideways scattered. This can be understood by a simple classical picture

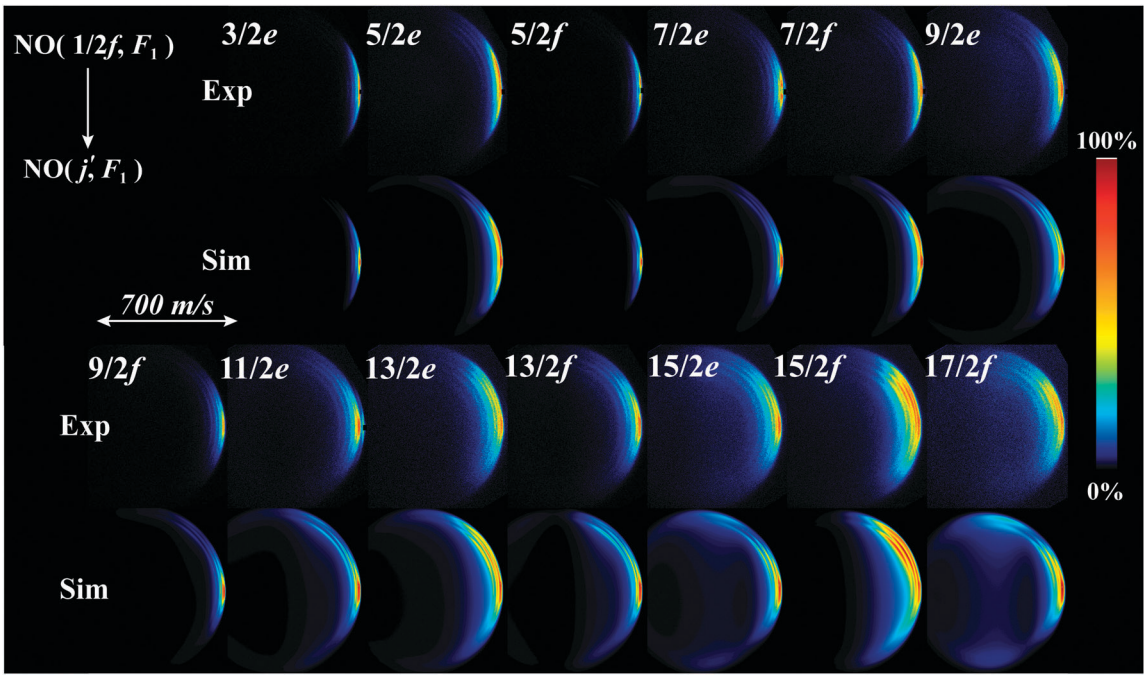

Fig. 5 Experimental (Exp) and corresponding simulated (Sim) images for the spin–orbit conserving ($F_1 \rightarrow F_1$) collisions of NO with O_2. Images are presented such that the forward direction appears on the right-hand side. Small segments of the images around the forward direction are masked because of imperfect state selection of the NO packet.

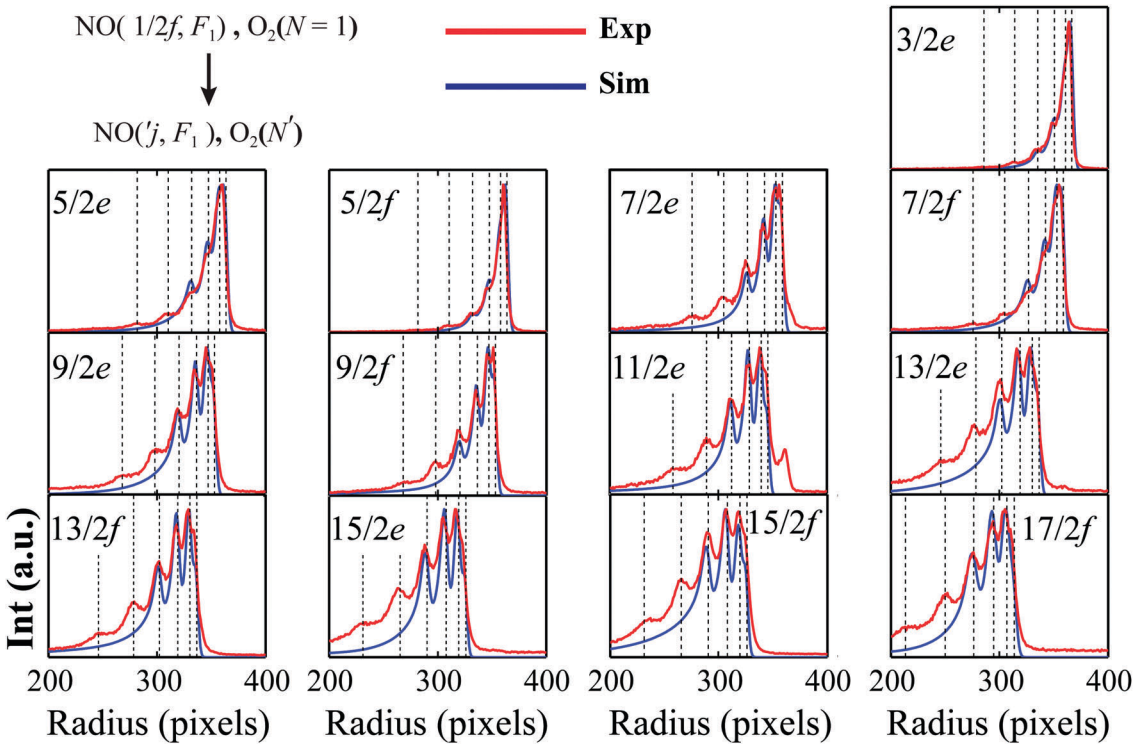

Fig. 6 Radial distributions derived from the experimental (Exp) and simulated images (Sim) from Fig. 5.

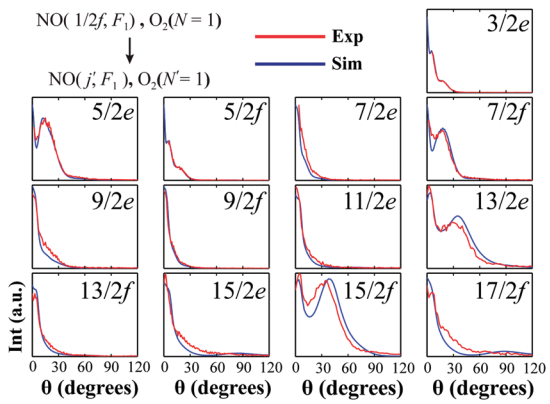

Fig. 7 Angular distributions derived from the experimental (Exp) and simulated images (Sim) from Fig. 5. Only the distributions for the outermost rings are shown, corresponding to elastic $N_{O_2} = 1 \rightarrow N'_{O_2} = 1$ collisions.

of RET, where low amounts of RET are associated with higher impact parameter, b, that tend to be forward scattered, while higher amounts of RET associated with smaller b tend to lead to sideways or backward scattering. Note that for certain final j'_{NO} states, a pronounced rainbow feature is observed that is in good agreement with theoretical predictions.

4.2 Spin–orbit changing transitions of NO

We now turn to spin–orbit changing $F_1 \rightarrow F_2$ transitions. Fig. 8–10 show the experimental and simulated scattering images, the radial distributions, and the angular distribution of the outermost $N_{O_2} = 1 \rightarrow N'_{O_2} = 1$ ring, respectively, for $F_1 \rightarrow F_2$ transitions as a function of j'_{NO}. As for the spin–orbit conserving $F_1 \rightarrow F_1$ transitions, the agreement between the experiment and simulation is excellent throughout. Similar trends are observed for $F_1 \rightarrow F_2$ transitions compared to $F_1 \rightarrow F_1$ transitions. Excitation of O_2 becomes stronger as the final rotational quantum number of NO, j'_{NO}, increases. The angular distribution of the scattered NO molecules shift from forward to sideways scattered as j'_{NO} increases. Rainbow features, however, are not observed for the scattering channels investigated here.

Although the $F_1 \rightarrow F_1$ and $F_1 \rightarrow F_2$ transitions show similar trends as a function of j'_{NO}, it is worth noting that spin–orbit changing transitions require more energy transfer for excitations with the same $\Delta j = j'_{NO} - j_{NO}$ when compared to spin–orbit conserving transitions. This offers the intriguing possibility to investigate whether the observed trends are governed predominantly by the transfer of angular momentum or rotational energy. Consider excitation to the rotational states 17/2f, F_1 and 5/2f, F_2 of NO. These states are almost energetically degenerate, although there is a significant difference in the angular momenta. The scattering images pertaining to these final states differ qualitatively significantly. For excitation to the 17/2f, F_1 level, O_2, scatters inelastically and the inner rings carry high intensity. By contrast, for excitation to the 5/2f, F_2 level, O_2 scatters predominantly elastically and the inner rings are less intense.

4.3 Interpretation

To interpret the observations, we analyze the scattering wave functions obtained from the coupled-channels calculations. These wave functions are validated by the comparison of

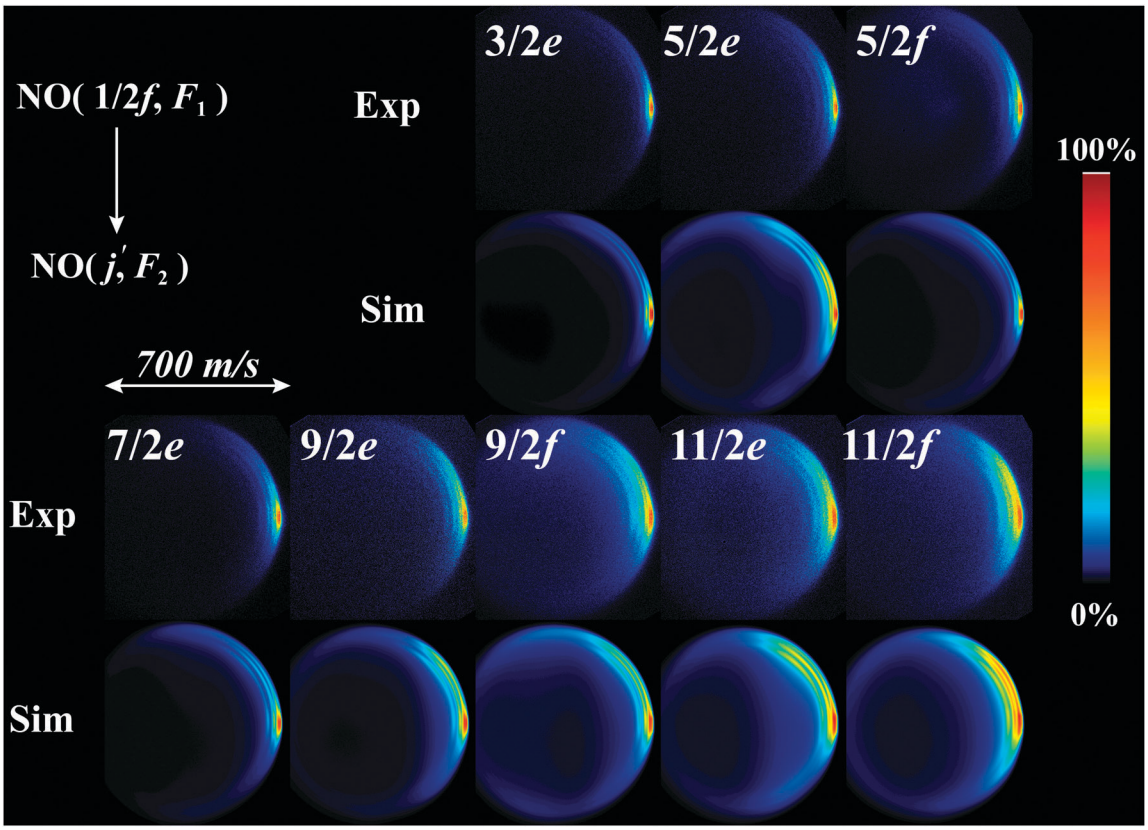

Fig. 8 Experimental (Exp) and corresponding simulated (Sim) images for the spin–orbit changing ($F_1 \rightarrow F_2$) collisions of NO with O_2. Images are presented such that the forward direction appears on the right-hand side.

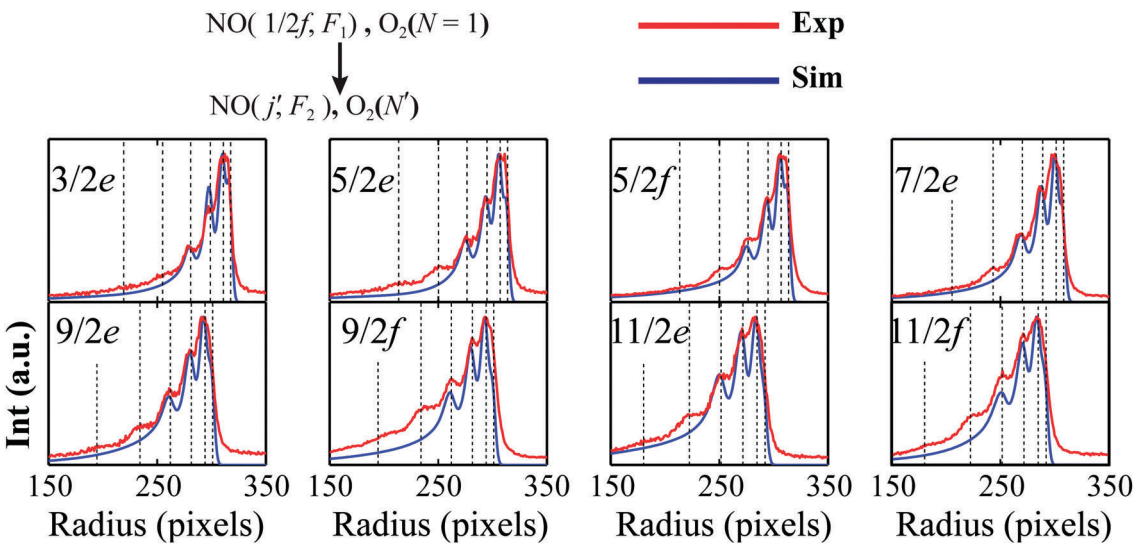

Fig. 9 Radial distributions derived from the experimental (Exp) and simulated images (Sim) from Fig. 8.

theoretical and experimental differential scattering cross sections, and the detailed analysis that the theoretical wave functions permit yields additional insight into the scattering dynamics. We analyze so-called opacity functions, which contain information on the range at which transitions occur, and the vector correlation of the angular momenta of the collisionally-excited molecules. A similar analysis has been performed in our previous study, at lower collision energies, and we here focus on the differences between spin–orbit conserving and changing transitions, which were not probed previously.[13]

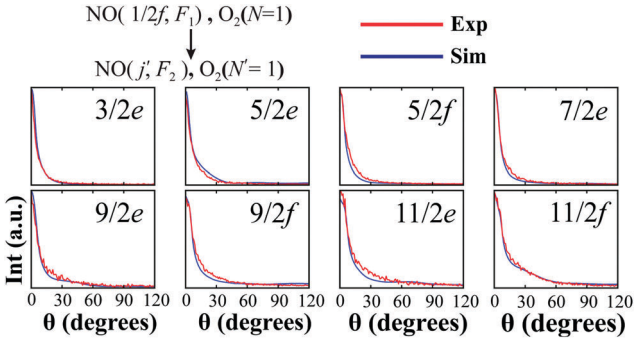

Fig. 10 Angular distributions derived from the experimental (Exp) and simulated images (Sim) from Fig. 8. Only the distributions for the outermost rings are shown, corresponding to elastic $N_{O_2} = 1 \rightarrow N'_{O_2} = 1$ collisions.

4.3.1 Opacity functions. The opacity function is defined as

$$P_{(i\rightarrow f)}(b) = \frac{k}{2\pi b}\sigma^{(\ell)}_{(i\rightarrow f)}, \quad (1)$$

where $b = \ell/k$ is the classical impact parameter and $\sigma^{(\ell)}_{(i\rightarrow f)}$ is the contribution of a single partial wave, ℓ, to the cross section for the transition from initial state i to final state f. The total cross section is given by

$$\sigma_{(i\rightarrow f)} = 2\pi\int_0^\infty P_{(i\rightarrow f)}(b)b\mathrm{d}b, \quad (2)$$

in the classical limit of continuous b, such that the opacity function, $P_{(i\rightarrow f)}$, can be thought of as the probability of a transition i → f for a collision occurring with well-defined classical impact parameter, b.

Fig. 11 shows the opacity plots for various spin–orbit conserving transitions of NO and the product pairs $N'_{O_2} = 1, 3, 5, 7$. For nearly elastic transitions, for both j'_{NO} and N'_{O_2}, there is a dominant contribution to the cross section by impact parameters larger than the classical turning point of the interaction potential, which occurs around $7a_0$. That is, the cross section is dominated by rotational excitation in glancing collisions, rather than head-on collisions. As either or both j'_{NO} and N'_{O_2} increases, the collision mechanism becomes more short ranged, and the cross section is dominated by impact parameters $b \lessapprox 7a_0$ for which the molecules collide head on. This is completely consistent with our previous study at lower collision energies.[13]

Fig. 12 shows similar opacity plots for spin–orbit changing transitions to the NO F_2 manifold. In this case, even for low j'_{NO} and N'_{O_2}, the cross sections are dominated by short-ranged collisions with impact parameters $b \lessapprox 7a_0$. This represents a surprising result as it shows that the range of the collision mechanism is governed by the amount of energy transferred, rather than by the amount of angular momentum transferred. The latter may have been expected as long-range interactions correspond to low rank terms in a tensorial expansion of the PES, and hence directly drive transitions with small changes in the monomer angular momenta only. In addition, the qualitative comparison between the channels that excite NO to the near-degenerate 17/2f, F_1 and 5/2f, F_2 levels, as described above, would have suggested that the amount of angular momentum transferred is more important than the amount of energy transferred.

4.3.2 Vector correlations of $\vec{j}_a$ and $\vec{j}_b$. We furthermore analyze the vector correlation of the angular momenta of the collisionally-excited molecules. This is accomplished by computing partial cross sections restricted to specific j_{AB} and j'_{AB}, the angular momentum quantum numbers associated with $\boldsymbol{j}_{AB} = \boldsymbol{j}_A + \boldsymbol{j}_B$, the vector sum of the monomer angular momenta. In the initial state,

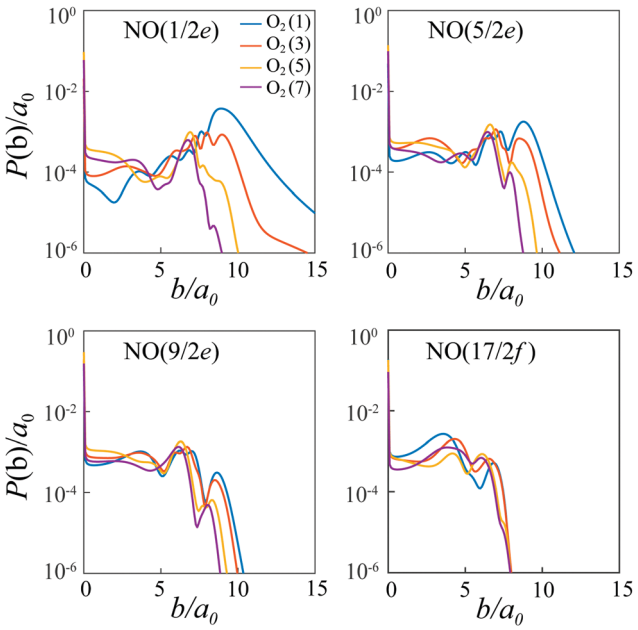

Fig. 11 Opacity plots for $O_2\left(N'_{O_2} = 1, 3, 5, 7\right)$ and fixed NO final states in the F_1, *i.e.*, for spin–orbit conserving transitions, as labeled in each panel.

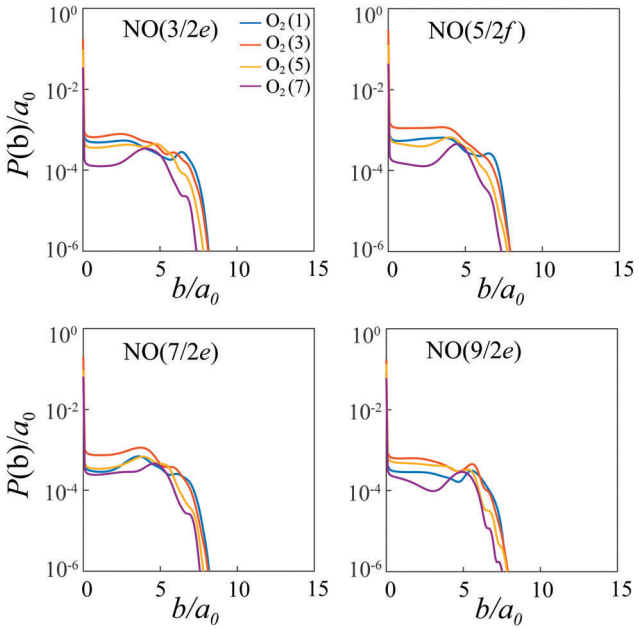

Fig. 12 Opacity plots for $O_2\left(N'_{O_2} = 1, 3, 5, 7\right)$ and fixed NO final states in the F_2, *i.e.*, for spin–orbit changing transitions, as labeled in each panel.

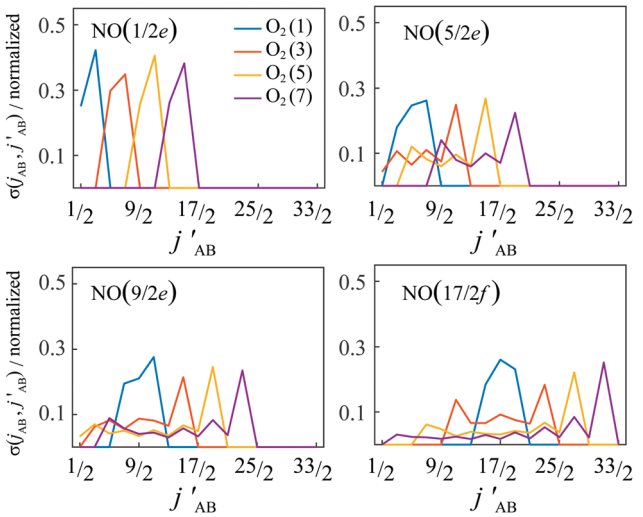

Fig. 13 Normalized partial cross sections for j_{AB} = 3/2 as a function of j'_{AB}. Each panel correspond to a fixed NO state and shows data for the four O_2 final states $N'_{O_2} = 1, 3, 5, 7$. All NO final states shown in this figure correspond to the F_1 spin–orbit manifold, *i.e*, this figure shows spin–orbit conserving transitions.

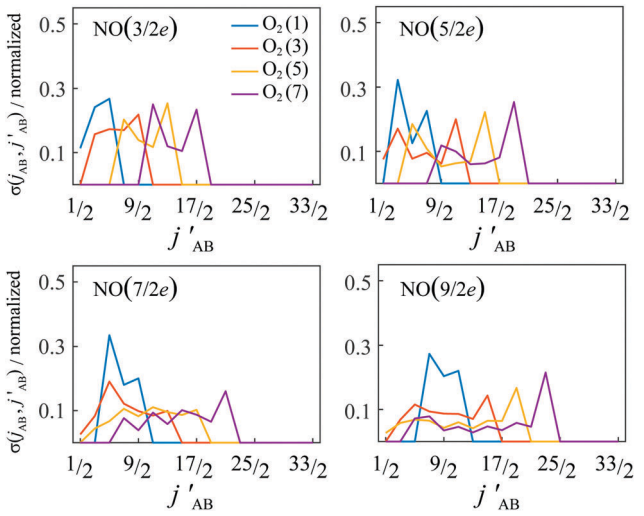

Fig. 14 Normalized partial cross sections for j_{AB} = 3/2 as a function of j'_{AB}. Each panel correspond to a fixed NO state and shows data for the four O_2 final states $N'_{O_2} = 1, 3, 5, 7$. All NO final states shown in this figure correspond to the F_2 spin–orbit manifold, *i.e*, this figure shows spin–orbit changing transitions.

j_{NO} = 1/2 and N_{O_2} = 1 such that j_{AB} is limited to the values j_{AB} = 1/2 and 3/2, by the triangular inequality. In the final state, the monomer angular momenta are larger and the quantum number j'_{AB} takes values between $j'^{min}_{AB} = \left|j'_{NO} - N'_{O_2}\right|$ and $j'^{min}_{AB} = j'_{NO} + N'_{O_2}$. If j'_{AB} assumes its maximum value, the monomer angular momenta are stretched or parallel to each other, whereas if j'_{AB} assumes its minimum value, the monomer angular momenta are anti-parallel. We note that this is a vector correlation of both monomer angular momenta relative to each other, but does not imply that either of the monomer angular momenta is oriented or aligned with respect to the scattering axis.

Fig. 13 shows the j_{AB} and j'_{AB}-restricted cross sections, for j_{AB} = 3/2 as a function of j'_{AB}, for various spin–orbit conserving transitions of NO. The partial cross sections are clearly peaked towards the highest value of j'_{AB} permitted by the triangular inequalities. This implies that there is a vector correlation of the monomer angular momenta such that the cross sections are dominated by stretched excited-state monomer angular momenta, which we discovered previously at lower collision energies.[13] This can be explained in a classical picture: if the colliding molecules exert equal and opposite forces, acting on the point of closest approach of the two molecules, this will induce a like torque on both molecules, such that the rotationally-excited molecules will exhibit the same sense of rotation, and the monomer angular momenta will be stretched (see Fig. 4 in ref. 13).

Fig. 14 similarly shows the j_{AB} and j'_{AB}-restricted cross sections, for j_{AB} = 3/2 as a function of j'_{AB}, for various transitions to the F_2 spin–orbit manifold of NO. In this case, the cross sections show no clear propensity for stretched monomer angular momenta, and no single value of j'_{AB} is seen to dominate the cross section. This behavior is expected as the above explanation – like torque induced by interactions acting on the point of closest approach – applies to pure rotational excitation. Instead, spin–orbit changing transitions are driven by the off-diagonal potential, which couples the $\Lambda = \pm 1$ NO substates, and is induced by non-adiabatic coupling between these asymptotically-degenerate substates.

5 Conclusions and outlook

We have presented high-resolution measurements of product pairs for inelastic collisions of state-selected NO radicals with O_2 molecules at a collision energy of 480 cm^{-1}. Both spin–orbit changing and spin–orbit conserving scattering channels were studied for a large number of final rotational states of NO. In general, the observations are in excellent agreement with the predictions of quantum mechanical coupled-channels scattering calculations, which are based on recently developed NO–O_2 PESs. For both spin–orbit conserving and changing transitions of NO, similar correlations of energy transfer in NO and O_2 were observed: the higher the energy uptake by NO, the higher probability that O_2 is excited to higher rotational states. Interesting differences were also observed. For spin–orbit conserving transitions, near-elastic collisions are dominated by glancing collisions at high impact parameters, whereas collisions with larger degree of inelasticity in either NO or O_2 become short ranged. By contrast, spin–orbit changing transitions are driven by head-on collisions associated with small impact parameters, even for low amounts of angular momentum transferred. Furthermore, the monomer angular momenta induced in spin–orbit conserving collisions describe a vector correlation, which can be understood classically. For spin–orbit changing transitions, the monomer angular momenta do not display this vector correlation.

Conflicts of interest

The authors declare no competing financial interest.

Acknowledgements

The research leading to these results has received funding from the European Research Council under the European Union's Seventh Framework Programme (FP7/2007–2013)/ERC grant agreement 335646 MOLBIL. This work is part of the research program of the Netherlands Organization for Scientific Research (NWO). The expert technical support by Niek Janssen, André van Roij, and Edwin Sweers is gratefully acknowledged.

References

1 A. T. J. B. Eppink and D. H. Parker, *Rev. Sci. Instrum.*, 1997, **68**, 3477–3484.
2 Y. T. Lee, *Science*, 1987, **236**, 793–798.
3 M. N. R. Ashfold, N. H. Nahler, A. J. Orr-Ewing, O. P. J. Vieuxmaire, R. L. Toomes, T. N. Kitsopoulos, I. A. Garcia, D. A. Chestakov, S.-M. Wu and D. H. Parker, *Phys. Chem. Chem. Phys.*, 2006, **8**, 26–53.
4 T. F. M. Luxford, T. R. Sharples, K. G. McKendrick and M. L. Costen, *J. Chem. Phys.*, 2017, **147**, 013912.
5 M. Brouard, S. D. S. Gordon, B. Nichols, E. Squires, V. Walpole, F. J. Aoiz and S. Stolte, *J. Chem. Phys.*, 2017, **146**, 204304.
6 E. A. Wade, K. T. Lorenz, J. L. Springfield and D. W. Chandler, *J. Phys. Chem. A*, 2003, **107**, 4976–4981.
7 O. Tkáč, M. Stei, A. J. Orr-Ewing and P. J. Dagdigian, *J. Chem. Phys.*, 2015, **142**, 014306.
8 A. Gijsbertsen, H. Linnartz and S. Stolte, *J. Chem. Phys.*, 2006, **125**, 133112.
9 C.-H. Yang, G. Sarma, D. H. Parker, J. J. ter Meulen and L. Wiesenfeld, *J. Chem. Phys.*, 2011, **134**, 204308.
10 O. Tkáč, A. K. Saha, J. Loreau, Q. Ma, P. J. Dagdigian, D. H. Parker, A. van der Avoird and A. J. Orr-Ewing, *Mol. Phys.*, 2015, **113**, 3925–3933.
11 O. Tkáč, C. A. Rusher, S. J. Greaves, A. J. Orr-Ewing and P. J. Dagdigian, *J. Chem. Phys.*, 2014, **140**, 204318.
12 Z. Gao, S. N. Vogels, M. Besemer, T. Karman, G. C. Groenenboom, A. van der Avoird and S. Y. T. van de Meerakker, *J. Phys. Chem. A*, 2017, **121**, 7446–7454.
13 Z. Gao, T. Karman, S. N. Vogels, M. Besemer, A. van der Avoird, G. C. Groenenboom and S. Y. T. van de Meerakker, *Nat. Chem.*, 2018, **10**, 469–473.
14 S. Y. T. van de Meerakker, H. L. Bethlem, N. Vanhaecke and G. Meijer, *Chem. Rev.*, 2012, **112**, 4828–4878.
15 C. Bieler, A. Sanov and H. Reisler, *Chem. Phys. Lett.*, 1995, **235**, 175–182.
16 J. A. Bacon, C. F. Giese and W. R. Gentry, *J. Chem. Phys.*, 1998, **108**, 3127–3133.
17 C. J. Eyles, M. Brouard, C.-H. Yang, J. Kłos, F. J. Aoiz, A. Gijsbertsen, A. E. Wiskerke and S. Stolte, *Nat. Chem.*, 2011, **3**, 597–602.
18 C. J. Eyles, M. Brouard, H. Chadwick, F. J. Aoiz, J. Kłos, A. Gijsbertsen, X. Zhang and S. Stolte, *Phys. Chem. Chem. Phys.*, 2012, **14**, 5420–5439.
19 A. Gijsbertsen, H. Linnartz, G. Rus, A. E. Wiskerke, S. Stolte, D. W. Chandler and J. Kłos, *J. Chem. Phys.*, 2005, **123**, 224305.
20 B. Nichols, H. Chadwick, S. D. S. Gordon, C. J. Eyles, B. Hornung, M. Brouard, M. H. Alexander, F. J. Aoiz, A. Gijsbertsen and S. Stolte, *Chem. Sci.*, 2015, **6**, 2202–2210.
21 M. Brouard, H. Chadwick, S. D. S. Gordon, B. Hornung, B. Nichols, F. J. Aoiz and S. Stolte, *J. Chem. Phys.*, 2016, **144**, 224301.
22 A. Gijsbertsen, H. Linnartz, C. A. Taatjes and S. Stolte, *J. Am. Chem. Soc.*, 2006, **128**, 8777–8789.
23 M. Brouard, H. Chadwick, S. D. S. Gordon, B. Hornung, B. Nichols, J. Kłos, F. J. Aoiz and S. Stolte, *J. Chem. Phys.*, 2014, **141**, 164306.
24 H. Chadwick, B. Nichols, S. D. S. Gordon, B. Hornung, E. Squires, M. Brouard, J. Kłos, M. H. Alexander, F. J. Aoiz and S. Stolte, *J. Phys. Chem. Lett.*, 2014, **5**, 3296–3301.
25 M. Brouard, H. Chadwick, S. D. S. Gordon, B. Hornung, B. Nichols, F. J. Aoiz and S. Stolte, *J. Chem. Phys.*, 2015, **119**, 12404–12416.
26 J. Onvlee, S. D. S. Gordon, S. N. Vogels, T. Auth, T. Karman, B. Nichols, A. van der Avoird, G. C. Groenenboom, M. Brouard and S. Y. T. van de Meerakker, *Nat. Chem.*, 2017, **9**, 226–233.
27 S. N. Vogels, J. Onvlee, S. Chefdeville, A. van der Avoird, G. C. Groenenboom and S. Y. T. van de Meerakker, *Science*, 2015, **350**, 787–790.
28 A. von Zastrow, J. Onvlee, S. N. Vogels, G. C. Groenenboom, A. van der Avoird and S. Y. T. van de Meerakker, *Nat. Chem.*, 2014, **6**, 216–221.
29 S. N. Vogels, J. Onvlee, A. von Zastrow, G. C. Groenenboom, A. van der Avoird and S. Y. T. van de Meerakker, *Phys. Rev. Lett.*, 2014, **113**, 263202.
30 M. Brouard, H. Chadwick, C. J. Eyles, B. Hornung, B. Nichols, F. J. Aoiz, P. G. Jambrina and S. Stolte, *J. Chem. Phys.*, 2013, **138**, 104310.
31 M. Brouard, H. Chadwick, C. J. Eyles, B. Hornung, B. Nichols, J. M. Scott, F. J. Aoiz, J. Kłos, S. Stolte and X. Zhang, *Mol. Phys.*, 2013, **111**, 1759–1771.
32 M. S. Westley, K. T. Lorenz, D. W. Chandler and P. L. Houston, *J. Chem. Phys.*, 2001, **114**, 2669–2680.
33 C. J. Eyles, M. Brouard, H. Chadwick, B. Hornung, B. Nichols, C.-H. Yang, J. Kłos, F. J. Aoiz, A. Gijsbertsen, A. E. Wiskerke and S. Stolte, *Phys. Chem. Chem. Phys.*, 2012, **14**, 5403–5419.
34 C. J. Eyles, M. Brouard, H. Chadwick, F. J. Aoiz, J. Kłos, A. Gijsbertsen, X. Zhang and S. Stolte, *Phys. Chem. Chem. Phys.*, 2012, **14**, 5420–5439.
35 S. D. Jons, J. E. Shirley, M. T. Vonk, C. F. Giese and W. R. Gentry, *J. Chem. Phys.*, 1996, **105**, 5397–5407.
36 S. D. Jons, J. E. Shirley, M. T. Vonk, C. F. Giese and W. R. Gentry, *J. Chem. Phys.*, 1992, **97**, 7831–7834.
37 H. Kohguchi, T. Suzuki and M. H. Alexander, *Science*, 2001, **294**, 832–834.

38 J. Onvlee, S. N. Vogels, A. von Zastrow, D. H. Parker and S. Y. T. van de Meerakker, *Phys. Chem. Chem. Phys.*, 2014, **16**, 15768–15779.
39 B. Yan, P. F. H. Claus, B. G. M. van Oorschot, L. Gerritsen, A. T. J. B. Eppink, S. Y. T. van de Meerakker and D. H. Parker, *Rev. Sci. Instrum.*, 2013, **84**, 023102.
40 M. Mizushima, *Theory of Rotating Diatomic Molecules*, John Wiley & Sons, New York, 1975.
41 C. M. Western, *J. Quant. Spectrosc. Radiat. Transfer*, 2017, **186**, 221–242.
42 T. Karman, A. van der Avoird and G. C. Groenenboom, *J. Chem. Phys.*, 2016, **144**, 121101.